HAL
open science

4D holographic microscopy of zebrafish larvae microcirculation

Dario Donnarumma, Alexey Brodoline, Daniel Alexandre, Michel Gross

To cite this version:

Dario Donnarumma, Alexey Brodoline, Daniel Alexandre, Michel Gross. 4D holographic microscopy of zebrafish larvae microcirculation. Optics Express, 2016, 24 (23), pp.26887-26900. 10.1364/OE.24.026887 . hal-01363227

HAL Id: hal-01363227

https://hal.science/hal-01363227v1

Submitted on 9 Sep 2016

HAL is a multi-disciplinary open access archive for the deposit and dissemination of scientific research documents, whether they are published or not. The documents may come from teaching and research institutions in France or abroad, or from public or private research centers.

L'archive ouverte pluridisciplinaire **HAL**, est destinée au dépôt et à la diffusion de documents scientifiques de niveau recherche, publiés ou non, émanant des établissements d'enseignement et de recherche français ou étrangers, des laboratoires publics ou privés.

4D holographic microscopy of zebrafish larvae microcirculation

Dario Donnarumma, Alexey Brodoline, Daniel Alexandre and Michel Gross*

Laboratoire Charles Coulomb - UMR 5221 CNRS-UM2 CC 026 Université Montpellier II
Place Eugêne Bataillon 34095 Montpellier cedex, France

**michel.gross@univ-montp2.fr*

Abstract: An original technique that combines digital holography, dual illumination of the sample and cleaning algorithm 3D reconstruction is proposed. It uses a standard transmission microscopy setup coupled with a digital holography detection. The technique is 4D, since it allows to determine, at each time step, the 3D locations (x, y, z) of many moving objects that scatter the dual illumination beam. The technique has been validated by imaging the microcirculation of blood in a fish larvae sample (the moving objects are thus red blood cells RBCs). Videos showing in 4D the moving RBCs superimposed with the perfused blood vessels are obtained.

© 2016 Optical Society of America

OCIS codes: (090.1995) Digital holography; (090.2880) Holographic interferometry; (180.3170) Interference microscopy; (290.5850) Scattering, particles.

References and links

1. E. Friedman, S. Krupsky, A. Lane, S. Oak, E. Friedman, K. Egan, and E. Gragoudas, "Ocular blood flow velocity in age-related macular degeneration," Ophthalmology **102**, 640–646 (1995).
2. M. P. Pase, N. A. Grima, C. K. Stough, A. Scholey, and A. Pipingas, "Cardiovascular disease risk and cerebral blood flow velocity," Stroke **43**, 2803–2805 (2012).
3. J. Kur, E. A. Newman, and T. Chan-Ling, "Cellular and physiological mechanisms underlying blood flow regulation in the retina and choroid in health and disease," Progress in retinal and eye research **31**,377–406 (2012).
4. O. Sakurada, C. Kennedy, J. Jehle, J. Brown, G. L. Carbin, and L. Sokoloff, "Measurement of local cerebral blood flow with iodo [14c] antipyrine," Am. J. Physiology-Heart and Circulatory Physiology **234**, H59–H66 (1978).
5. I. Kanno, H. Iida, S. Miura, M. Murakami, K. Takahashi, H. Sasaki, A. Inugami, F. Shishido, and K. Uemura, "A system for cerebral blood flow measurement using an h215o autoradiographic method and positron emission tomography," J. Cerebral Blood Flow & Metabolism **7**, 143–153 (1987).
6. Y. Yeh and H. Cummins, "Localized fluid flow measurements with an he-ne laser spectrometer," Appl. Phys. Lett. **4**, 176–178 (1964).
7. J. D. Briers and S. Webster, "Laser speckle contrast analysis (lasca): a nonscanning, full-field technique for monitoring capillary blood flow," J. Biomed. Opt. **1**, 174–179 (1996).
8. A. K. Dunn, "Laser speckle contrast imaging of cerebral blood flow," An. Biomedical Engineering **40**, 367–377 (2012).
9. D. Briers, D. D. Duncan, E. Hirst, S. J. Kirkpatrick, M. Larsson, W. Steenbergen, T. Stromberg, and O. B. Thompson, "Laser speckle contrast imaging: theoretical and practical limitations," J. Biomed. Opt. **18**, 066018–066018 (2013).
10. S. Yuan, A. Devor, D. A. Boas, and A. K. Dunn, "Determination of optimal exposure time for imaging of blood flow changes with laser speckle contrast imaging," Appl. Opt. **44**, 1823–1830 (2005).
11. Y. Zeng, M. Wang, G. Feng, X. Liang, and G. Yang, "Laser speckle imaging based on intensity fluctuation modulation," Opt. Lett. **38**, 1313–1315 (2013).
12. D. Gabor, "A new microscopic principle," Nature **161**, 777–778 (1948).
13. E. N. Leith and J. Upatnieks, "Reconstructed wavefronts and communication theory," J. Opt. Soc. Am. A **52**, 1123–1128 (1962).

14. U. Schnars and W. Jüptner, "Direct recording of holograms by a ccd target and numerical reconstruction," Appl. Opt. **33**, 179–181 (1994).
15. M. Atlan, M. Gross, P. Desbiolles, É. Absil, G. Tessier, and M. Coppey-Moisan, "Heterodyne holographic microscopy of gold particles," Opt. lett. **33**, 500–502 (2008).
16. S.-H. Lee, Y. Roichman, G.-R. Yi, S.-H. Kim, S.-M. Yang, A. van Blaaderen, P. van Oostrum, and D. G. Grier, "Characterizing and tracking single colloidal particles with video holographic microscopy," Opt. Express **15**, 18275–18282 (2007).
17. F. C. Cheong, B. J. Krishnatreya, and D. G. Grier, "Strategies for three-dimensional particle tracking with holographic video microscopy," Opt. Express **18**, 13563–13573 (2010).
18. J. Gao, J. A. Lyon, D. P. Szeto, and J. Chen, "In vivo imaging and quantitative analysis of zebrafish embryos by digital holographic microscopy," Biomed. Opt. Express **3**, 2623–2635 (2012).
19. N. Verrier, D. Alexandre, and M. Gross, "Laser doppler holographic microscopy in transmission: application to fish embryo imaging," Opt. Express **22**, 9368–9379 (2014).
20. F. Saglimbeni, S. Bianchi, A. Lepore, and R. Di Leonardo, "Three-axis digital holographic microscopy for high speed volumetric imaging," Opt. Express **22**, 13710–13718 (2014).
21. J. Högbom, "Aperture synthesis with a non-regular distribution of interferometer baselines," Astronomy and Astrophysics Supplement Series **15**, 417 (1974).
22. F. Soulez, L. Denis, C. Fournier, É. Thiébaut, and C. Goepfert, "Inverse-problem approach for particle digital holography: accurate location based on local optimization," J. Opt. Soc. Am. A **24**, 1164–1171 (2007).
23. F. Soulez, L. Denis, E. Thiébaut, C. Fournier, and C. Goepfert, "Inverse problem approach in particle digital holography: out-of-field particle detection made possible," J. Opt. Soc. Am. A **24**, 3708–3716 (2007).
24. F. Le Clerc, L. Collot, and M. Gross, "Numerical heterodyne holography with two-dimensional photodetector arrays," Opt. Lett. **25**, 716–718 (2000).
25. M. Westerfield, "The Zebrafish Book: a Guide for the Laboratory use of Zebrafish (Danio rerio)" (Institute of Neuroscience. University of Oregon, 1995).
26. S. Isogai, M. Horiguchi, and B. M. Weinstein, "The vascular anatomy of the developing zebrafish: an atlas of embryonic and early larval development," Developmental biology **230**, 278–301 (2001).
27. N. Warnasooriya, F. Joud, P. Bun, G. Tessier, M. Coppey-Moisan, P. Desbiolles, M. Atlan, M. Abboud, and M. Gross, "Imaging gold nanoparticles in living cell environments using heterodyne digital holographic microscopy." Opt. Express **18**, 3264–73 (2010).
28. F. Verpillat, F. Joud, P. Desbiolles, and M. Gross, "Dark-field digital holographic microscopy for 3d-tracking of gold nanoparticles," Opt. Express **19**, 26044–26055 (2011).
29. N. Verrier, D. Alexandre, G. Tessier, and M. Gross, "Holographic microscopy reconstruction in both object and image half-spaces with an undistorted three-dimensional grid," Appl. Opt. **54**, 4672–4677 (2015).
30. E. Cuche, P. Marquet, and C. Depeursinge, "Spatial filtering for zero-order and twin-image elimination in digital off-axis holography," Appl. Opt. **39**, 4070–4075 (2000).
31. L. Yu and M. K. Kim, "Wavelength-scanning digital interference holography for tomographic three-dimensional imaging by use of the angular spectrum method," Opt. lett. **30**, 2092–2094 (2005).

1. Introduction

Blood flow i maging techniques are widely used in bio-medical studies, since they can assess physiological processes or can be used for early detection of disease [1–3]. However, many blood flow studies require, for imaging purposes, the use of a contrast agent, making blood flow characterization invasive [4, 5]. Scanning Doppler imaging techniques can be considered to alleviate this issue, but due to the scanning step, acquisition of an image is a time consuming process [6]. By analyzing the spatial statistics of the dynamic speckle with the Laser Speckle Contrast Analysis/Imaging (LASCA/LSCI) technique [7] the blood flow can be imaged [8, 9]. Improvement of the acquired contrast image has been achieved through exposure time optimization [10], or intensity fluctuation analysis [11] resulting in high quality perfusion images. However, these techniques are limited to perfusion monitoring in 2D and unable to reconstruct the structure of the blood flow in 3D.

Proposed by Gabor [12] and improved by Leith and Upatnieks [13] holography records the interference of the field scattered by an object with a known reference field. It is then possible to extract, from this interference pattern, the scattered field that reaches the holographic detector. This is particularly easy in digital holography that uses a camera detector. Holography is intrinsically a 3D technique since the Maxwell equations can be used to back propagate the

field from the camera to any point of the 3D space [14]. This allows to localize and track a point-like object that scatters light, since its position coincides with the maximum of intensity of the reconstructed field [15]. The localization accuracy along the z axis depends strongly on the experimental conditions, in particular on the detection numerical aperture. Nanometric accuracy can be reached in holographic microscopy with a high numerical aperture (NA ≥ 1) objective [16, 17].

Digital holography has been used to image and qualitatively analyze blood flows in 2D [18, 19]. 3D holographic imaging of blood flow is challenging for a number of reasons. The biologically relevant size of the microcirculation makes it impossible to use a high NA objective, since the field of view would be too small. Blood cells are much larger than the wavelength, and their refractive index is close to the plasma one. The light is then scattered within a small angle in the forward direction. In transmission geometry, this corresponds to a small NA and to a low z accuracy. In reflection geometry, this leads to a low signal, which competes with light scattered by the surrounding living tissues, whose refractive index is not homogeneous in time and space.

In this paper, we have imaged in 3D moving red blood cells (RBCs) in a living fish larvae. We used an original technique that combines digital holography, illumination of the sample and reconstruction along several axis [20], and calculations that involve both standard holographic propagation and 3D reconstruction by a cleaning algorithm [21–23]. More specifically, the experiment was developed with an holographic microscopy setup working in transmission. To increase the angle diversity of the light scattered by the sample, the illumination was made by two beams that were angularly tilted with respect to the optical axis. At each time point, the difference of successive images was calculated yielding 2-frame holograms that contain information on the light that is scattered by the moving objects (i.e. the RBCs) at that time. Two holograms, that describe the field components of each illumination beam, were then extracted from the data. These two holograms were used to calculate the two scattered fields 3D maps corresponding to each illumination. Since these two maps describe the scattering made by the same RBCs, they must exhibit correlation maximums in locations (x, y, z) that correspond to RBCs. We used thus these correlation maximums to calculate the 3D map of the RBC locations. We got then 3D videos of the moving RBCs and, by averaging, 3D images of perfused blood vessels.

2. Experimental setup

Our holography set-up is similar to the one of the reference [19] (see Fig. 1). The set-up uses an upright microscope (Olympus® CX41) that has been modified to perform heterodyne holography [24] in transmission. The main laser (HL6545MG: 60 mW @ $\lambda = 660$ nm, optical frequency ω_I) is split into two arms (illumination and reference) by a beam splitter BS. Two acousto-optic modulators (AOM) at $\omega_{1,2}/2\pi \simeq 80$ MHz control the frequency ω_{LO} of the reference (i.e. local oscillator) field E_{LO}:

$$\omega_{LO} = \omega_I + \omega_1 - \omega_2 \tag{1}$$

The illumination arm (field E) is split into two branches so as to illuminate the sample in two directions, whose relative angle is 28.3°. The sample is a zebrafish larvae (150 hours-old) between slide and cover slip. It is imaged with a microscope objective MO (NA= 0.30, G=10). To achieve off-axis holography, the beam splitter that recombines the signal (E) and reference (E_{LO}) fields is angularly tilted: ($\theta \neq 0$). The camera (Mikrotron Eosens CL: 1280×1024 pixels, $\omega_{CAM}/2\pi = 220$ Hz, 10 bits, 14 μm square pitch) records the signal versus reference interference pattern $I_m = |E + E_{LO}|^2$, where $m = 0...M$ (with $M = 128$ to 1024) is the frame or

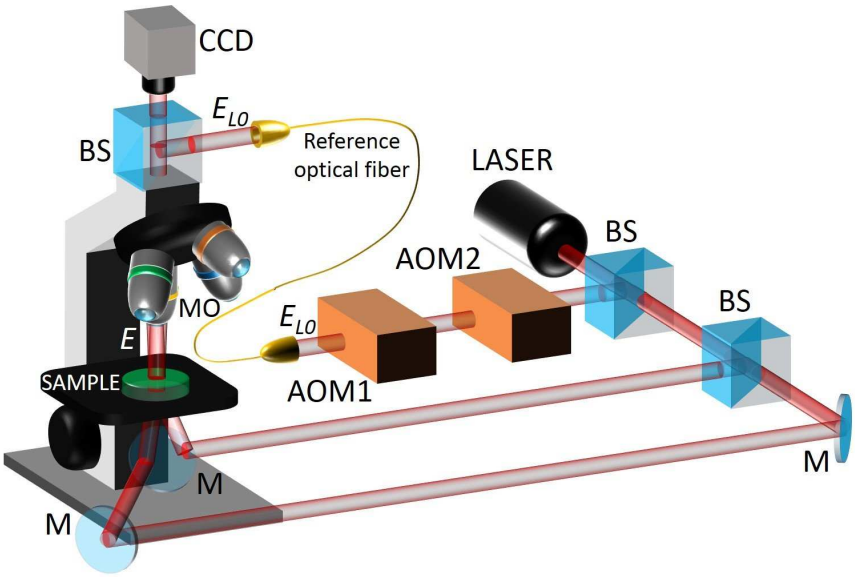

Fig. 1. Heterodyne digital holographic microscopy experimental arrangement. AOM1, AOM2: acousto-optic modulators (Bragg cells) that shift the frequency of the local oscillator beam; MO: microscope objective; M: mirror; BS: angularly tilted cube beam splitter. E and E_{LO}: signal and reference complex fields.

time index. The recorded data are cropped into a 1024×1024 calculation grid to perform the holographic calculations involving digital Fourier transforms (FFT).

Zebrafishes (Danio rerio, wild type AB line) were maintained according to standard protocols [25]. Larvae were mounted on a standard glass slide under a 22 mm 1.5 round coverslip. A 0.5 mm thick caoutchouc ring served as a spacer and sealant. They were embedded in a drop of cooling 1.5% low melting point agarose at 37°C and oriented before gelation. The chamber was filled with 100 mg/l tricaine in filtered tank water and imaging was performed at room temperature. Blood vessels nomenclature is according to [26].

3. Data filtering and reconstruction.

3.1. 4 phase reconstruction of the MO pupil image and selection of the signal corresponding to each illumination direction

We first performed a test experience, in which the field scattered by the sample is detected by 4 phases heterodyne holography. The detection is then made at the illumination frequency, and the holographic signal corresponds to the field scattered by immobile or almost immobile scatterers of the sample (ground glass or zebrafish larvae). The resulting signal is strong and allows for precise optical adjustment of our holographic device. This test experiment is also useful to illustrate the reconstruction procedure.

This procedure is similar to the one used in previous works [27, 28] (for details see [29]), but with small differences due to the double illumination, and to the need of selecting the signals corresponding to each illumination. In the test experiment, we tuned the LO frequency ω_{LO} to perform 4 phase detection, and we considered 4 phase holograms $H_{4\varphi}$. We have thus:

$$\begin{aligned} \omega_{LO} &= \omega_I + \omega_{CAM}/4 \\ H_{4\varphi} &= [I_0 - I_2] \; + \; j\,[I_1 - I_3] \end{aligned} \tag{2}$$

where $I_0, I_1 \ldots I_3$ are consecutive camera frames, and $j^2 = -1$. To select the +1 holographic grating order and to compensate for the MO pupil phase curvature, we performed the holographic reconstruction of the MO pupil by the Schnars et al. method [14] yielding $\tilde{H}_{4\varphi}(k_x, k_y)$ with:

$$\tilde{H}_{4\varphi}(k_x, k_y) \quad = \quad \mathrm{FFT}\left[\, H_{4\varphi}(x,y)\; e^{jk(x^2+y^2)/2d} \,\right] \tag{3}$$

where FFT is the discrete Fourier transform operator, and k is the modulus of the wave-vector: $k = 2\pi/\lambda$. Here, $e^{jk(x^2+y^2)/2d}$ is the quadratic phase factor that determines the reconstruction plane. It depends on the curvature of the reference wave front, and on the distance from the camera to the reconstruction plane. Note that a phase quadratic in k_x and k_y that affects $H_{4\varphi}$ is missing in Eq. (2) (with respect to the Schnars et al. work [14]). This missing phase does not affect the intensity images $|\tilde{H}_{4\varphi}(k_x, k_y)|^2$.

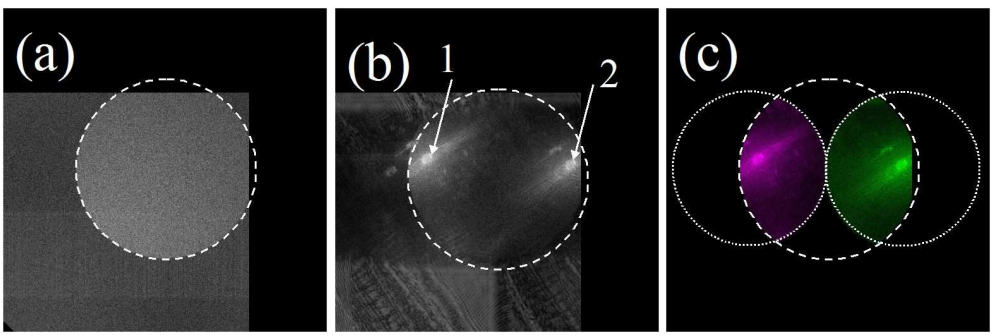

Fig. 2. (a, b) Zoom of the upper right hand corner of the intensity images $|\tilde{H}_{4\varphi}(k_x, k_y)|^2$ obtained with 4-phase holograms by reconstructing the MO pupil plane. (c) Fourier space hologram obtained after translation of the selected zone in the center of the calculation grid. The purple and green zones correspond to the holograms related to each illumination direction. The sample is a ground glass (a) or zebrafish sample (b,c).

Figures 2(a) and 2(b) show the reconstructed images of the pupil. The display is made in arbitrary log scale for intensity: $|\tilde{H}_{4\varphi}|^2$. Images are obtained with a ground glass (Fig. 2(a)) and with a living zebrafish sample (Fig. 2(b)). Figure 2(a) exhibits a circular zone whose brightness is high and homogeneous. This zone corresponds to the image of the MO pupil that is back illuminated through the ground glass. The brightness is homogeneous because the ground glass scatters light over angles wider than the MO collection angle. Because of the off-axis configuration (angular tilt θ of BS), the pupil image is located in the upper right side of the calculation grid, but it is displayed in the center of Fig. 2(a). Note that diffusers do not move in the ground glass experiment. It results that the scattered field E does not vary with time, and that the 4-phase demodulation made by Eq. (2) selects the +1 grating order term, since we have: $H_{4\varphi} = E^*_{LO} E$. The -1 and 0 grating order images, that are zero, are not visible in Fig. 2(a).

To get the images of Fig. 2, the reconstruction parameter d (used to calculate the phase factor $e^{jk(x^2+y^2)/2d}$ of Eq. (3)) has been adjusted to perform the reconstruction in the MO pupil plane. As seen, the pupil image exhibits sharp edges (white dashed line circle). The useful holographic

information was then selected by cropping the pupil zone and by filling the remaining of the calculation grid with zeros. This corresponds to the Cuche et al. spatial filtering of the +1 grating order term EE_{LO}^{*} [30]. To compensate for the off-axis angular tilt, the cropped zone was translated into the center of the calculation grid.

Figure 2(b) was obtained by imaging a zebrafish sample. Because the sample was quite transparent, the two illumination beams yield two bright spots, which are well separated in the Fourier space (see arrows 1 and 2 in Fig. 2(b)). Around the spots, we can see two blurred brighter regions corresponding to the light scattered by the sample. Since these brighter regions are well separated, we extracted, from the holographic data $\tilde{H}_{4\varphi}$, two holograms $\tilde{H}_{\text{purple}}$ and $\tilde{H}_{\text{green}}$ that describe the field scattered from each illumination direction. This was done by cropping, within $\tilde{H}_{4\varphi}$, two circular zones of radius 240 pixels centered on each spot (dotted white circle in Fig. 2(c)) yielding the two holograms $\tilde{H}_{\text{purple}}$ and $\tilde{H}_{\text{green}}$ (see purple and green zones in Fig. 2(c)). Note that all the scattered light has been caught by either $\tilde{H}_{\text{purple}}$ or $\tilde{H}_{\text{green}}$. The selection of the illumination direction was thus done without loss of information.

3.2. Holographic reconstruction of the field scattered by the circulating RBCs

In order to select the signal from moving RBCs, we considered 2-phase holograms $H_{2\varphi}$ recorded without frequency shift of the LO beam.

$$\begin{aligned} \omega_{LO} &= \omega_I \\ H_{2\varphi} &= I_0 - I_1 \end{aligned} \tag{4}$$

The signal resulting from an object that is not moving is not taken into account in $H_{2\varphi}$. The images that are reconstructed from $H_{2\varphi}$ correspond then to the moving components of the sample, i.e. to RBCs. $\tilde{H}_{2\varphi}$ is calculated similarly to $\tilde{H}_{4\varphi}$ by:

$$\tilde{H}_{2\varphi}(k_x,k_y) = \text{FFT}\left[e^{jk(x^2+y^2)/2d}H_{2\varphi}(x,y)\right] \tag{5}$$

Because $H_{2\varphi}(x,y)$ is real, $\tilde{H}_{2\varphi}$ exhibits both the +1 and -1 order images. Nevertheless, because of the off-axis configuration, these two images do not overlap. The +1 image is thus selected by cropping the pupil zone (whose exact location has been determined previously by the ground glass experiment), and by translating this zone into the center of the calculation grid. By this way, the useful holographic information is selected and the off-axis angular tilt is compensated. To separate the signals of the two illuminations, we performed, like in section 3.1, two crops of radius 240 pixels centered on the two illumination spots of Fig. 2(c). We obtained the two Fourier space holograms $\tilde{H}_{\text{purple}}(k_x,k_y)$ and $\tilde{H}_{\text{green}}(k_x,k_y)$, from which we have calculated the two holograms $H_{\text{purple}}(x,y)$ and $H_{\text{green}}(x,y)$:

$$\begin{aligned} H_{\text{purple}}(x,y) &= \text{FFT}^{-1}\tilde{H}_{\text{purple}}(k_x,k_y) \\ H_{\text{green}}(x,y) &= \text{FFT}^{-1}\tilde{H}_{\text{green}}(k_x,k_y) \end{aligned} \tag{6}$$

where FFT^{-1} is the reverse Fourier transform operator. The holograms $H_{\text{purple}}(x,y,z)$ and $H_{\text{green}}(x,y,z)$, reconstructed in planes z, are then calculated by the angular spectrum method [31]. This method involves two Fourier transforms from the real space holograms $H_{\text{purple}}(x,y)$ and $H_{\text{green}}(x,y)$, but only one Fourier transform from the Fourier space holograms $\tilde{H}_{\text{purple}}(k_x,k_y)$ and $\tilde{H}_{\text{green}}(k_x,k_y)$. We have:

$$
\begin{aligned}
H_{\text{purple}}(x,y,z) &= \text{FFT}^{-1} e^{-j(k_x^2+k_y^2)z/2k} \tilde{H}_{\text{purple}}(k_x,k_y) \\
H_{\text{green}}(x,y,z) &= \text{FFT}^{-1} e^{-j(k_x^2+k_y^2)z/2k} \tilde{H}_{\text{green}}(k_x,k_y)
\end{aligned} \tag{7}
$$

where FFT is the discrete Fourier transform operator. Here, x, y and k_x, k_y are discrete coordinates whose pitches are Δx and Δk, which obey to $N\,\Delta x\,\Delta k = 2\pi$ where $N = 1024$ is the size of the calculation grid.

Up to now, we have considered that both acquisition and reconstruction were made in the image half-space (near the camera). The pitches are then $\Delta x = D_{pix}$ and $\Delta k = 2\pi/(ND_{pix})$ (where $D_{pix} = 14\ \mu$m is the size of the camera pixels). x, y and z are the coordinates of the image of the sample (that is conjugated with the sample by MO). This point of view, which is most often adopted in the literature, is not very convenient, since we want to reconstruct the scattered fields with coordinates related to the sample.

A better point of view [29] is to consider that both acquisition and reconstruction are made in the object half-space (i.e. near the sample). $H_{2\varphi}(x,y)$ is then the hologram recorded in the plane of the object half-space that is conjugated with the camera by MO. All the mathematical transformations made to calculate $H_{\text{purple}}(x,y)$ and $H_{\text{green}}(x,y)$ yield holograms, whose phases are properly corrected (i.e. the phase of the hologram is the same as the phase of the field). Equation (7) performs then the reconstruction with orthogonal coordinates x, y and z that correspond to the real coordinates near the sample. The pitches are $\Delta x = D_{pix}/G$, $\Delta k = 2\pi G/(ND_{pix})$, where G is the imaging gain from the plane $z = 0$ to the camera. Note that G is generally not equal to the objective nominal gain ($\times 10$ here), since it depends on the exact location of the camera with respect to MO. The best is to measure the gain G by a calibration procedure.

In analyzing our data, we have considered the second point of view. We have measured G by imaging a USAF target. This calibration yields $G = 24.6$, $\Delta x = 14\ \mu\text{m}/24.6 = 0.569\ \mu$m and $\Delta k = 2\pi/(1024\Delta x)$.

4. Dual illumination reconstructed images and videos

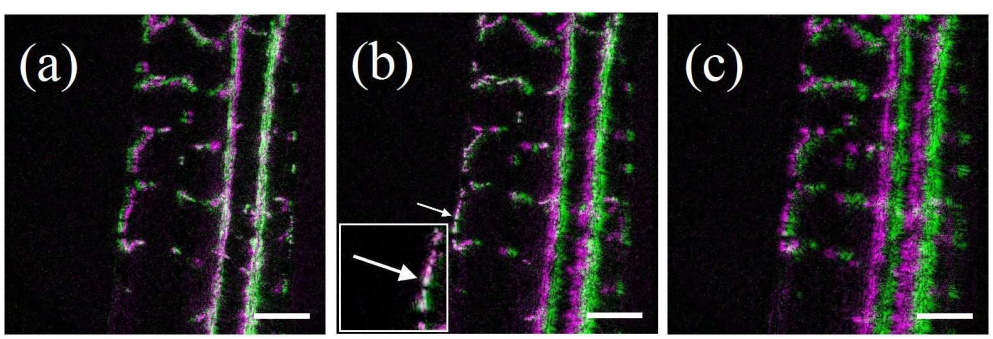

Fig. 3. Reconstructed intensity image of RBCs made with the 2-phase hologram $H_{2\varphi,m}$ (see Eq. (4)) where the time index is $m = 77$. The purple and green components $H_{\text{purple},m}(x,y,z)$ and $H_{\text{green},m}(x,y,z)$ of the images were obtained by selecting the purple and the green zones of Fig. 2(c). Reconstruction was made with $z = -26.7$ (a), $z = 0$ (b) and $z = +26.7\ \mu$m (c). The displayed images (a..c) correspond to image 77 of file Visualization 1 (a), Visualization 2 (b) and Visualization 3 (c). Dorsal side left, anterior to the top. Bar is 100 μm.

We imaged a zebrafish sample by recording, without frequency shift of the LO beam ($\omega_{LO} = \omega_I$), a sequence of frames I_m (with $m = 1...129$). With each couple of consecutive

frames: I_m and I_{m+1}, we calculated the 2-phase holograms $H_{2\varphi,m} = I_m - I_{m+1}$. With each hologram $H_{2\varphi,m}$, we calculated $H_{\text{purple},m}(x,y,z)$ and $H_{\text{green},m}(x,y,z)$ by Eqs. (5)–(7). The video files Visualization 1, Visualization 2 and Visualization 3 show the intensity reconstructed images, whose components are $|H_{\text{purple},m}(x,y,z)|^2$ and $|H_{\text{green},m}(x,y,z)|^2$, that were obtained, for $m = 1$ to 128, and for respectively $z = 0$, $z = +26.7$ and $z = 53.5$ μm.

The images 77 (time index $m = 77$) of these video files are displayed on Figs. 3(a)-3(c). In figure 3 (a), the reconstructed plane $z = 0$ corresponds to the locations of the caudal vein and caudal artery. Indeed, the purple and green components of the caudal vein and caudal artery images are superimposed yielding white patterns. In figure 3(b), with $z = 26.7$ μm, the large parallel longitudinal vessels (caudal vein and caudal artery) are out of the reconstruction plane, and the purple and green components are well separated. On the other hand, the dorsal capillary seen in the bottom left side of the image is within the reconstruction plane, and the purple and green images of the RBC pointed by the arrow coincides (see zoom in Fig. 3(b)). In figure 3 (b), with $z = 53.5$ μm, the purple and green components of both the caudal vein, caudal artery and dorsal capillaries are separated.

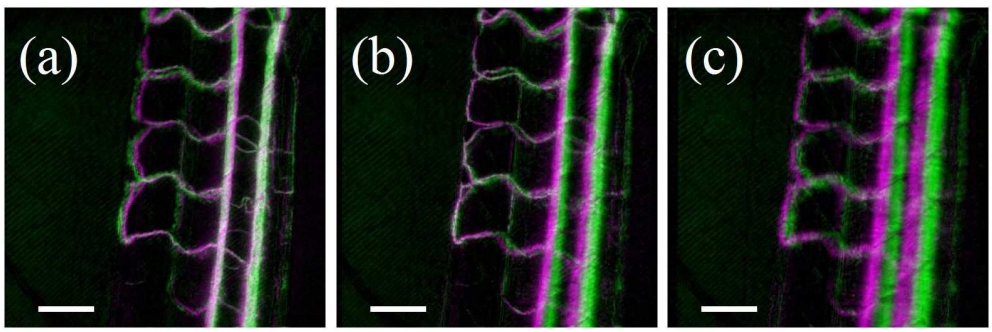

Fig. 4. Averaged intensity reconstructed images made with 2 phases holograms: $H_{2\varphi,m} = I_m - I_{m-1}$ and with $\omega_1 = \omega_2$. The purple and green components $\langle|H_{\text{purple}}(x,y,z)|^2\rangle$ and $\langle|H_{\text{green}}(x,y,z)|^2\rangle$ are calculated with Eq. (8). Reconstruction was made with $z = 0$ (a), $z = +26.7$ (b) and $z = +53.5$ μm (c). The displayed images correspond to image 51 (a), 76 (b) and 101 (c) of file Visualization 4. Bar is 100 μm.

To image the inside structure of the perfused blood vessels, corresponding to the entire trajectories of the RBCs along the observation time, we calculated the averaged intensity holograms $\langle|H_{\text{purple}}|^2\rangle$ and $\langle|H_{\text{green}}|^2\rangle$:

$$\langle|H_{\text{purple}}(x,y,z)|^2\rangle = (1/128)\sum_{m=0}^{127}|H_{\text{purple},m}(x,y,z)|^2 \quad (8)$$

$$\langle|H_{\text{green}}(x,y,z)|^2\rangle = (1/128)\sum_{m=0}^{127}|H_{\text{green},m}(x,y,z)|^2 \quad (9)$$

The video file Visualization 4 shows the averaged intensity reconstructed images, whose components are $\langle|H_{\text{purple}}(x,y,z)|^2\rangle$ and $\langle|H_{\text{green}}(x,y,z)|^2\rangle$. These images are obtained for $z = -53.5$ to $z = +53.5$ μm in 101 steps of 1.07 μm. Figure 4 shows the averaged intensity reconstructed images obtained for $z = 0$ (a), $z = +26.7$ (b) and $z = +53.5$ μm (c).

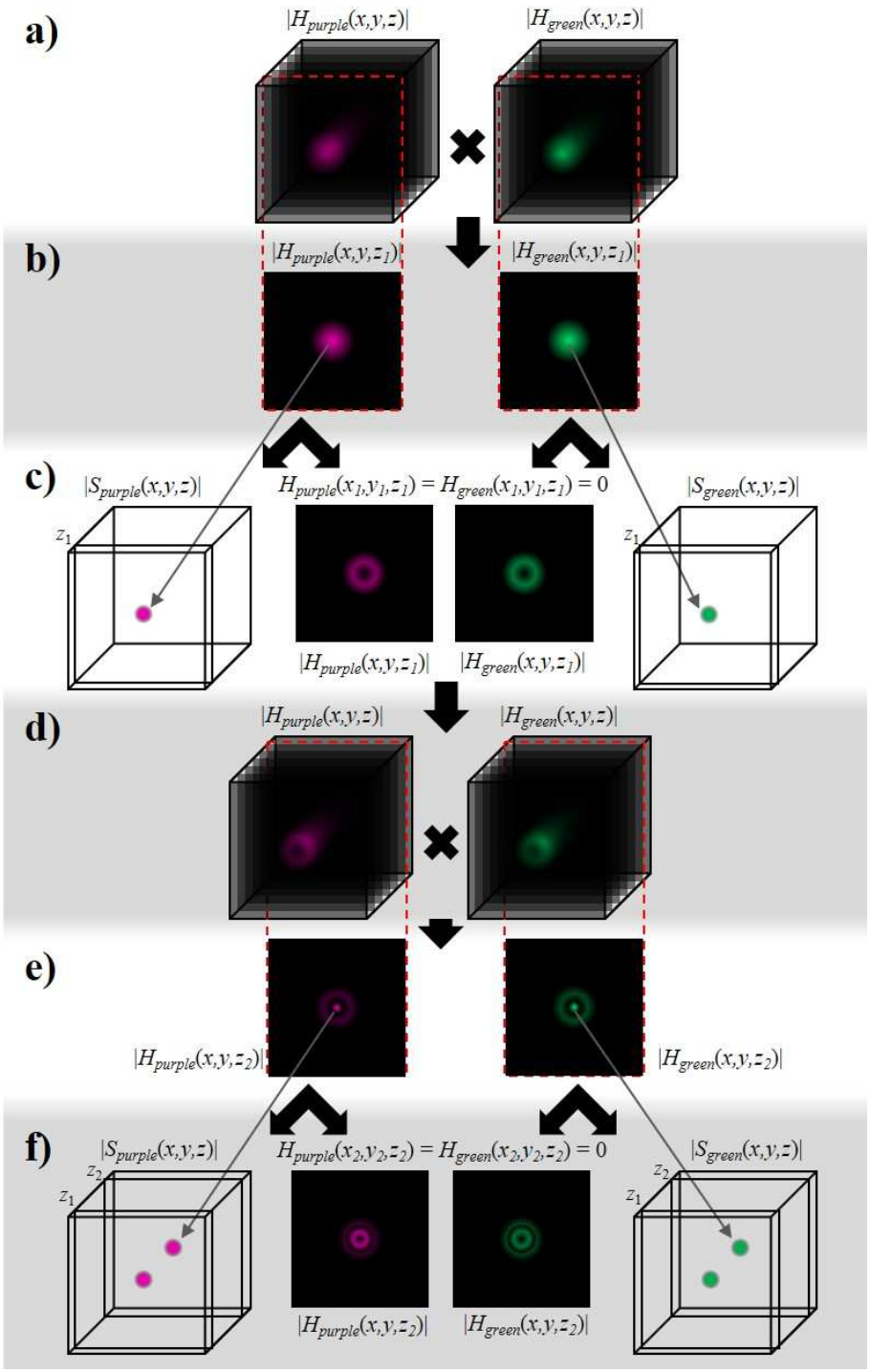

Fig. 5. Scheme of the 3D reconstruction process by the cleaning algorithm. In (a) the product between the two 3D grids is calculated. This allows to select, in (b), the point of highest correlation $x_1; y_1; z_1$. Thus, in (c), the point is stored in $S_{\text{purple}}(x,y,z)$ and $S_{\text{green}}(x,y,z)$ and erased from $|H_{\text{purple}}(x,y,z_1)|$ and $|H_{\text{green}}(x,y,z_1)|$. From this modified plane, in (d) the overall grid is recalculated. In (e) a new maximum correlation point $x_2; y_2; z_2$ is found. Again, in (f), new sources are stored in the associated space of sources and set to zero in the plane $z = z_2$ of the 3D grid. A new cycle will start and the operation will be repeated K times.

5. 3D reconstruction by a cleaning algorithm

The intensity maps $|H_{\text{purple},m}(x,y,z)|^2$ and $|H_{\text{green},m}(x,y,z)|^2$ are not quantitative 3D representations of the scatterers (i.e the RBCs), but are sequences of 2D images of the field scattered by the RBCs in different z planes, as showed in Fig.6(a). $|H_{\text{purple},m}(x,y,z)|^2$ corresponds to the purple beam that is scattered, while $|H_{\text{green},m}(x,y,z)|^2$ corresponds to the green beam. It's only by comparing the signal scattered by the purple and green beams that we determined the 3D location of each RBC, and obtain thus a 3D image of the sample (see Fig.6(b)) at the time t_m, where t_m is the recording time of frame m.

To calculate the RBCs locations at time step m, we considered that both holograms H_{purple} and H_{green} result from a sum of K fields, scattered by K sources of field $S_{\text{purple},k}$ and $S_{\text{green},k}$ (with $k = 1...K$) that describe the scattering of the two beams by the RBC scatterer of index k. We consider thus here single scattering of K independent sources. The holograms H_{purple} and H_{green} result thus from two 3D maps of the sources S_{purple} and S_{green} that scatter the illumination field:

$$\begin{aligned} S_{\text{purple}}(x,y,z) &= \sum_{k=1}^{K} S_{\text{purple},k}(x,y,z) \\ S_{\text{green}}(x,y,z) &= \sum_{k=1}^{K} S_{\text{green},k}(x,y,z) \end{aligned} \tag{10}$$

Note that we have considered here that sources S_{purple} and S_{green} are highly correlated, since they represent the same scatterers.

In the calculations, we have considered a 3D calculation grid of $512 \times 512 \times 128$ points in x, y and z, and $K = 25000$ RBC scatterers. This figure ($K = 25000$) corresponds to about 10% of the area of the calculation grid 512×512. The pitch is $2 \times 0.569 = 1.138$ μm in x and y and 0.68 μm in z. Moreover, we have considered RBCs scatterers whose cross section is one pixel. $S_{\text{purple},k}$ and $S_{\text{green},k}$ are thus zero everywhere except in the location of the kth RBC that is (x_k, y_k, z_k). Let's describe with more details the calculation algorithm we have used. This algorithm is illustrated by Fig. 5.

1. At each time step m, we first calculate the coordinates (x_1, y_1, z_1) of the 1^{rst} RBC. This is done by calculating $H_{\text{purple}}(x,y,z)$ and $H_{\text{green}}(x,y,z)$ for the $512 \times 512 \times 128$ points of the 3D grid: see Fig. 5(a). We assume then that the location (x_1, y_1, z_1) of the 1^{rst} RBC corresponds to a coincidence in the holographic signals H_{purple} and H_{green}. Since the phase of the scattered fields strongly depends on the illumination direction, we consider intensities. We thus calculate the intensity product $\left(|H_{\text{purple}}|^2 \times |H_{\text{green}}|^2\right)$ in all points of the 3D grid, and say that the maximum of this product is reached in point (x_1, y_1, z_1). We then consider the 2D holograms $H_{\text{purple}}(x,y,z_1)$ and $H_{\text{green}}(x,y,z_1)$ in plane z_1 (Fig. 5(b)), and we split them in two components (Fig. 5(c)):

$$\begin{aligned} H_{\text{purple}}(x,y,z_1) &= H_{\text{purple},1}(x,y,z_1) + S_{\text{purple},1}(x,y,z_1) \\ H_{\text{green}}(x,y,z_1) &= H_{\text{green},1}(x,y,z_1) + S_{\text{green},1}(x,y,z_1) \end{aligned} \tag{11}$$

The first 2D components $S_{\text{purple},1}$ and $S_{\text{green},1}$ describe the field scattered by the first RBC. In plane z_1, $S_{\text{purple},1}$ and $S_{\text{green},1}$ are zero except in point x_1, y_1, where they are equal to H_{purple} and H_{green}. On the other hand, $H_{\text{purple},1}$ and $H_{\text{green},1}$ describe the fields scattered by the other RBCs. In plane z_1, $H_{\text{purple},1}$ and $H_{\text{green},1}$ are zero in point x_1, y_1, and equal to H_{purple} and H_{green} in the other points.

2. We then calculate the location (x_2, y_2, z_2) of the second RBC by using $H_{\text{purple},1}$ and $H_{\text{green},1}$, which are known in plane z_1. This is done by calculating $H_{\text{purple},1}$ and $H_{\text{green},1}$ in all points of the 3D calculation grid, and by assuming that the maximum of $\left(|H_{\text{purple},1}|^2 \times |H_{\text{green},1}|^2\right)$ is reached in point (x_2, y_2, z_2): see Fig. 5(d). The holograms $H_{\text{purple},1}$ and $H_{\text{green},1}$ in plane z_2 (Fig. 5(e)) are split again in two components (Fig. 5(f)).

$$\begin{aligned} H_{\text{purple},1}(x,y,z_2) &= H_{\text{purple},2}(x,y,z_2) + S_{\text{purple},2}(x,y,z_2) \\ H_{\text{green},1}(x,y,z_2) &= H_{\text{green},2}(x,y,z_2) + S_{\text{green},2}(x,y,z_2) \end{aligned} \tag{12}$$

$S_{\text{purple},2}$ and $S_{\text{green},2}$ correspond to the second RBC, while $H_{\text{purple},2}$ and $H_{\text{green},2}$ to RBCs of index $k = 3...K$. The algorithm used here is cleaning, because the field sources $S_{\text{purple},1}$ and $S_{\text{green},1}$ of the first RBC have been removed from the holographic data $H_{\text{purple},1}$ and $H_{\text{green},1}$ that are used to calculate the holographic sources $S_{\text{purple},k\geq 2}$ and $S_{\text{green},k\geq 2}$ of the other RBCs.

3. The following steps are similar to steps one and two. We calculate the location (x_k, y_k, z_k) of the kth RBC by using $H_{\text{purple},k-1}$ and $H_{\text{green},k-1}$, which are known in plane z_{k-1}. $H_{\text{purple},k-1}$, $H_{\text{green},k-1}$ are then calculated in all points. Maximum of $\left(|H_{\text{purple},k-1}|^2 \times |H_{\text{green},k}|^2\right)$ yields (x_k, y_k, z_k). The holograms $H_{\text{purple},k-1}$ and $H_{\text{green},k-1}$ in plane z_k are split:

$$\begin{aligned} H_{\text{purple},k-1}(x,y,z_k) &= H_{\text{purple},k}(x,y,z_k) + S_{\text{purple},k}(x,y,z_k) \\ H_{\text{green},k-1}(x,y,z_k) &= H_{\text{green},k}(x,y,z_2) + S_{\text{green},k}(x,y,z_k) \end{aligned} \tag{13}$$

We get then the sources $S_{\text{purple},k}$ and $S_{\text{green},k}$ and the holograms $H_{\text{purple},k}$ and $H_{\text{green},k}$ needed to continue the calculation.

4. We get $S_{\text{purple},k}$ and $S_{\text{green},k}$ for $k = 1...K$ i.e. for all RBCs. $S_{\text{purple},k}$ and $S_{\text{green},k}$ are then summed together by Eq. (10) yielding the 3D maps $S_{\text{purple}}(x,y,z)$ and $S_{\text{green},k}(x,y,z)$.

5. The calculation of S_{purple} and S_{purple} described above at time t_m is made for all 2-phase holograms $H_{2\varphi,m}$ of the sequence. The S_{purple} and S_{green} maps are thus calculated in 4D, with coordinates $x, y, z, t = t_m$.

The calculation described above is quite heavy. To get the location of the kth RBC scatterer, we must calculate the location of the maximum of $|H_{\text{purple},k}|^2 \times |H_{\text{purple},k}|^2$. It requires $2 \times 128 = 256$ discrete Fourier transforms (FFTs) of 512×512 points, to get $H_{\text{purple},k-1}$ and $H_{\text{green},k-1}$ in all the z planes of the $512 \times 512 \times 128$ calculation grid, plus some work to calculate $|H_{\text{purple},k}|^2 \times |H_{\text{purple},k}|^2$ for all points, and to determine the location of the maximum. To get S_{purple} and S_{green} at each time step t_m, one need to locate $K = 25000$ RBCs scattered whose area is 1 pixel. This requires $256 \times 2.5\ 10^4 = 6.4\ 10^6$ FFTs, plus some other work. This calculation was done in about 80 mn with a NVidia GTX TITAN Graphics Processing Unit (GPU). In the video files presented further, we have consider sequences of $m = 1...122$ holograms. The GPU calculation was made in about 122×80 mn, i.e. 7 days.

6. The 3D map of the scatterers obtained by the cleaning algorithm

In order to illustrate how the dual illumination scheme and the cleaning algorithm quantitatively enhance the z-axis confinement of 3D blood vessel structures, we have displayed, in Fig. 6,

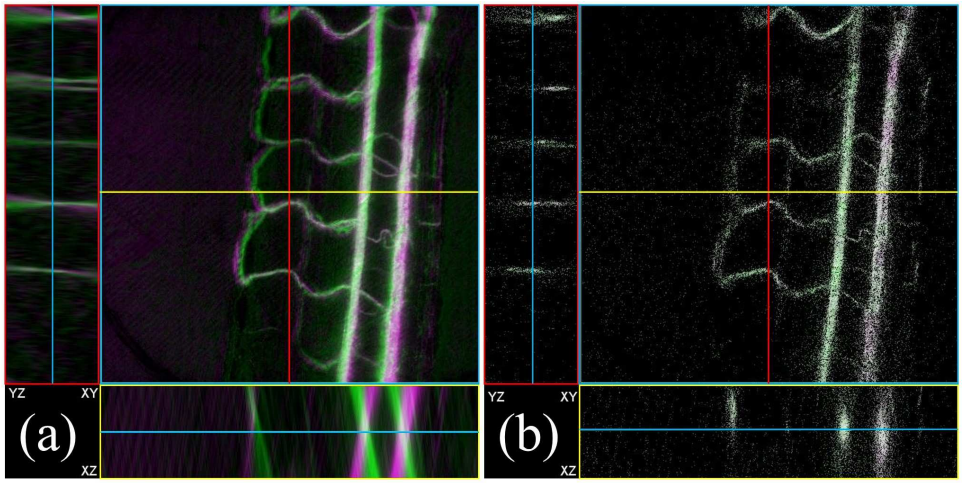

Fig. 6. Results of the 3D reconstruction made without (a) and with (b) the cleaning algorithm. (a) cuts of $\langle |H_{\text{purple}}(x,y,z)|^2 \rangle$ and $\langle |H_{\text{green}}(x,y,z)|^2 \rangle$ along the planes XY (upper-right image highlighted in blue), YZ (upper-left, red) and XZ (lower, yellow). (b) cuts of $\langle |S_{\text{purple},\theta}|^2 \rangle$ and $\langle |S_{\text{green},\theta}|^2 \rangle$ along the planes XY, YZ and XZ. In (a) and (b) the cuts correspond respectively to images 64 of the video file Visualization 5 and Visualization 6. The blue, red and yellow lines represent the relative positions of the planes XY, YZ and XZ.

the XY, YZ and XZ cuts of the averaged reconstructed 3D maps obtained without and with the cleaning algorithm i.e. $\langle |H_{\text{purple}}(x,y,z)|^2 \rangle$ and $\langle |H_{\text{green}}(x,y,z)|^2 \rangle$ (without) and $\langle |S_{\text{purple}}(x,y,z)|^2 \rangle$ and $\langle |S_{\text{green}}(x,y,z)|^2 \rangle$ (with).

Without cleaning (see Fig. 6 (a)), the z confinement is poor. In the XZ and YZ cuts, the green and purple images of the blood vessels are angularly tilted, and the location of the vessels corresponds to the z location where the green and purple images coincide. With cleaning (see Fig. 6 (b)), the z confinement is much better. Since the green and purple images coincide, the images are displayed in white. The 3D maps obtained without and with cleaning are also displayed in the video files Visualization 5 and Visualization 6 (x, y and z are swept in 128 steps of pitch $8\Delta x$ and Δz). To image a quite large zone of the zebrafish blood vessel structure, the experiment was made with a NA=0.3 microscope objective. The purple versus green axis angle is thus lower than in [20] (see xz cut of Fig. 6 (a)), and the z confinement is thus lower too.

Note that the RBCs are much larger than one voxel, but, to keep all useful information, the cleaning algorithm was made by considering one voxel scatterers. $K = 25000$ corresponds thus to the number of voxels that is considered in the cleaning algorithm. This figure is enough to handle most of the scattered energy, and thus to image all the RBCs, whose number is much lower than K.

7. Visualization of the data calculated by the cleaning algorithm

The visualization of the 4D maps S_{purple} and S_{green} calculated by the cleaning algorithm is challenging, because of the 4 coordinates. To perform visualization, we have projected the instantaneous intensities $|S_{\text{purple}}|^2$ and $|S_{\text{green}}|^2$ (that are 3D maps of real numbers) along the direction $\mathbf{u}_\theta = (\cos\theta, 1, \sin\theta)$ yielding, for each time step m and each direction $\mathbf{u}_\theta$, 2D images that can be displayed. The projections are defined by:

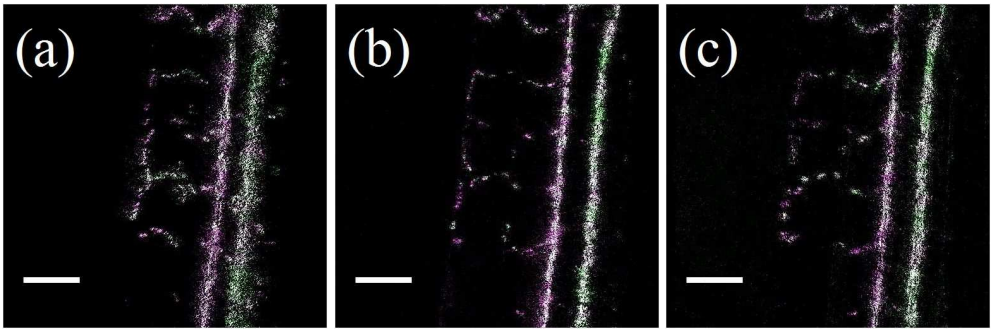

Fig. 7. Instantaneous projections $|S_{\text{purple},\theta}|^2$ and $|S_{\text{green},\theta}|^2$. The projections correspond to images 1, 32 and 46 of the video file Visualization 7, i.e. to time $m = 1$ and angle $\theta = -30^\circ$ (a), $m = 32$ and $\theta = 0^\circ$ (b), and $m = 46$ and $\theta = +15^\circ$ (c). The display is made in arbitrary logarithmic scale: $|S_{\text{purple},\theta}|^2$ is displayed in purple, $|S_{\text{green},\theta}|^2$ in green. Bar is 100 μm.

$$
\begin{aligned}
|S_{\text{purple},\theta}(x,y,t_m)|^2 &= \sum_z |S_{\text{purple}}(x\cos\theta + z\sin\theta, y, z, t_m)|^2 \\
|S_{\text{green},\theta}(x,y,t_m)|^2 &= \sum_z |S_{\text{green}}(x\cos\theta + z\sin\theta, y, z, t_m)|^2
\end{aligned}
\tag{14}
$$

We have displayed the projection $|S_{\text{purple},\theta}|^2$ in purple and $|S_{\text{green},\theta}|^2$ in green in a video file of 122 images (Visualization 7), where the time index varies from $m = 1$ to 122 in 122 steps, while the angle varies from $\theta = -30^\circ$ to $+30^\circ$ in 61 steps, and from $\theta = +30^\circ$ to -30° in 61 steps. Figure 7 shows the images 1, 32 and 46 of the file Visualization 7, which correspond to time $m = 1$ and projection angle $\theta = -30^\circ$ (a), $m = 32$ and $\theta = 0^\circ$ (b), $m = 46$ and $\theta = +15^\circ$ (c). The individual RBCs and its 3D motion can be seen in the video file.

It should be stressed that the cleaning algorithm is nonlinear, in the sense that it emphasizes the moving scatterers, whose signal is highest, which happen to be here the RBCs. Lower contributions to the signal such as vasomotion have not been detected.

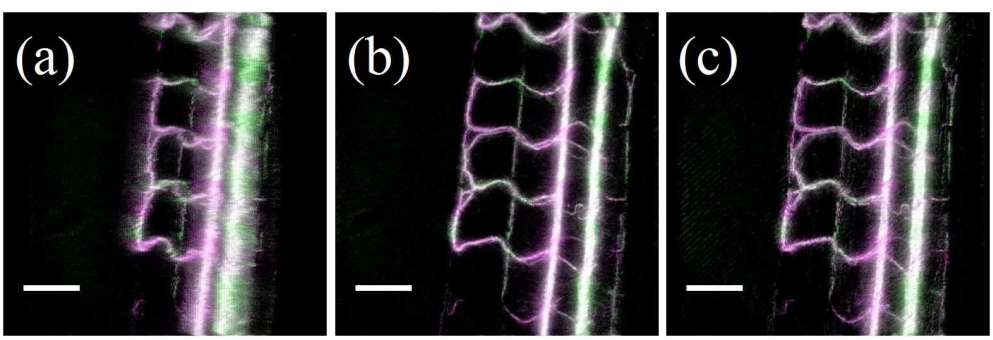

Fig. 8. Averaged projection $\langle|S_{\text{purple},\theta}|^2\rangle$ and $\langle|S_{\text{green},\theta}|^2\rangle$. The projections correspond to images: 1, 41 and 61 of the video file Visualization 8 i.e. to time $m = 1$ and angle $\theta = -40^\circ$ (a), $m = 1$ and $\theta = 0^\circ$ (b), and $\theta = +20^\circ$ (c). The display is made in arbitrary logarithmic scale: $\langle|S_{\text{purple},\theta}|^2\rangle$ is displayed in purple, $\rangle|S_{\text{green},\theta}|^2\rangle$ in green. Bar is 100 μm.

To visualize the entire trajectories of the RBCs, that correspond to the inside of the per-

fused blood vessels, we have calculated the time averaged intensity holograms $\langle |H_{\text{purple}}|^2 \rangle$ and $\langle |H_{\text{green}}|^2 \rangle$. We got:

$$\begin{aligned} \langle |S_{\text{purple},\theta}(x,y)|^2 \rangle &= \frac{1}{122} \sum_{m=1}^{122} |S_{\text{purple},\theta}(x,y,t_m)|^2 \\ \langle |S_{\text{green},\theta}(x,y)|^2 \rangle &= \frac{1}{122} \sum_{m=1}^{122} |S_{\text{green},\theta}(x,y,t_m)|^2 \end{aligned} \tag{15}$$

We have displayed $\langle |S_{\text{purple},\theta}|^2 \rangle$ and $\langle |S_{\text{green},\theta}|^2 \rangle$ in a video file of 162 images (Visualization 8), where the angle varies from $\theta = -40°$ to $+40°$ in 81 steps, and from $\theta = +40°$ to $-40°$ in 81 steps. Figure 7 shows the images 1 (a), 41 (b) and 61 (c) of file Visualization 8, which correspond to $\theta = -40°$ (a), $\theta = 0°$ (b), and $\theta = +20°$ (c). The 3D character of the blood vessels is clearly seen in the video file since the images of the blood vessels depends on the projection angle θ.

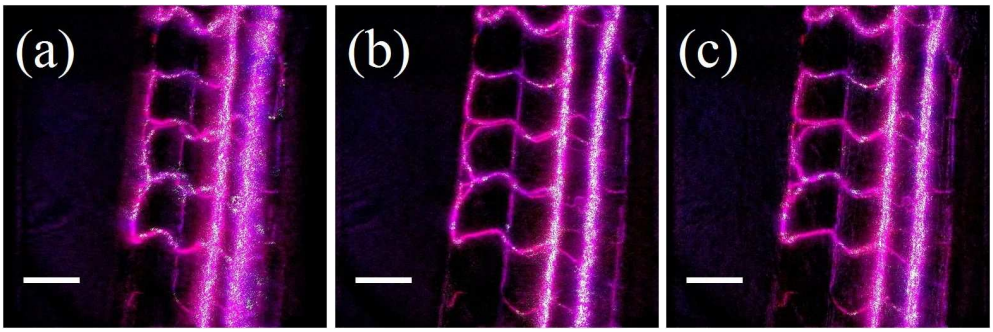

Fig. 9. Averaged projections $\langle |S_{\text{purple},\theta}|^2 \rangle$ and $\langle |S_{\text{green},\theta}|^2 \rangle$ superimposed with the instantaneous projections $|S_{\text{purple},\theta}|^2$ and $|S_{\text{green},\theta}|^2$. The projections correspond to images 1, 32 and 46 of file Visualization 9, i.e. to time index $m = 1$ and projection angle $\theta = -30°$ (a), $m = 32$ and $\theta = 0°$ (b), $m = 46$ and $\theta = +15°$ (c). The display is made in arbitrary logarithmic scale: $\langle |S_{\text{purple},\theta}|^2 \rangle$ is displayed in purple, $\rangle |S_{\text{green},\theta}|^2 \rangle$ in green. Bar is 100 μm.

To better visualize the 3D character of the motion of the RBCs, we have superimposed in a video file (Visualization 9) the averaged projections $\langle |S_{\text{purple},\theta}|^2 \rangle$ and $\langle |S_{\text{green},\theta}|^2 \rangle$ that show the perfused blood vessels, with the instantaneous projections $|S_{\text{purple},\theta}|^2$ and $|S_{\text{green},\theta}|^2$ that show the motion of individuals RBCs. In the video file Visualization 9, the time index varies from $m = 1$ to 122 in 122 steps, while the angle varies from $\theta = -30°$ to $+30°$ in 61 steps, and from $\theta = +30°$ to $-30°$ in 61 steps. The projections are displayed in arbitrary logarithmic scale: the averaged projections $\langle |S_{\text{purple},\theta}|^2 \rangle$ and $\langle |S_{\text{green},\theta}|^2 \rangle$ are displayed in blue and red, while the instantaneous projections $|S_{\text{purple},\theta}|^2$ and $|S_{\text{green},\theta}|^2$ are both displayed in green. With this choice of colors, the blood vessels are seen in purple, while the individual RBCs are white. Figure 9 shows the images 1 (a) , 32 (b) and 46 (c) of file Visualization 9, which correspond to time index $m = 1$ and projection angle $\theta = -30°$ (a), $m = 32$ and $\theta = 0°$ (b), $m = 46$ and $\theta = +15°$ (c). The 3D character of the blood vessels is clearly seen in the video file. The 3D character of the RBCs motion is seen visible. As expected, the RBCs follow the blood vessels paths.

8. Conclusion

In this paper, we proposed an original imaging technique that combines a digital holographic microscopy setup with dual illumination of the sample, and calculations involving both stan-

dard holographic reconstruction and 4D calculations by a cleaning algorithm. The setup uses an upright microscope that has been transformed into an heterodyne holographic device [24] working in transmission. The holograms H_{purple} and H_{green} that correspond to the scattering of each illumination beams were extracted from the camera recorded data I_m. By making the hypothesis that the two holograms H_{purple} and H_{green} were generated by the same scatterers (i.e. the moving red blood cells), the location of the scatterers (x_k, y_k and z_k) and their complex scattering amplitudes S_{purple} and S_{green} were calculated by a cleaning algorithm. The amplitudes S_{purple} and S_{green} are 4D data (x, y, z and t) that were used to generate video files showing in 4D the RBCs (Visualization 7), the blood vessels (Visualization 8) and the RBCs superimposed with the blood vessels (Visualization 9).

In comparison with other techniques dedicated to monitor in vivo blood flow, including laser Doppler and laser speckle, the proposed approach has the major advantage, specifically thanks to the recording of holograms, to be able to measure 3D aspects of the RBC movements. The proposed method can be still improved by using a more efficient cleaning algorithm for the 3D reconstruction and a setup allowing a larger angle of separation of the two illuminations beams. These improvements should yield faster calculations and higher z resolution. Future work should allow to calculate 3D maps of velocity vectors by analyzing H_{purple} and H_{green} at successive instants of time t_m and t_{m+1}.

Funding

Labex Numev (convention ANR-10-LABX-20) . Grant Number: 2014-1-042

Acknowledgments

We aknoledge O. Strauss for fruitful discussions and NVIDIA Corporation for the donation of the GTX Titan GPU.